ORIGINAL ARTICLE

Coupling mechanisms of static and dynamic loads during the ultrasonic impact strengthening of Ti-6Al-4V

Xuming Zha[1,2] · Zhi Yuan[1] · Hao Qin[1] · Linqing Xi[1] · Bicheng Guo[1] · Tao Zhang[3] · Feng Jiang[4]

Abstract
The ultrasonic impact-strengthening technology was used to effectively improve the fatigue resistance of the key components, which could be attributed to the association of static and dynamic impact loads. It is widely used in the high-performance manufacturing of critical aerospace components, such as titanium alloys. During the ultrasonic impact-strengthening process, the static and dynamic loading can provide two different deformation mechanisms, which may cause differences in the strengthening effect of the titanium alloys. This study developed an ultrasonic impact-strengthening test platform to investigate the influence mechanisms of static loads and cyclic dynamic impact loads in the ultrasonic impact-strengthening process. Meanwhile, the experiment platform was based on displacement control and could apply either static loads or cyclic dynamic impact loads individually on the surface of the Ti-6Al-4V. The force values in the static load experiments, cyclic dynamic impact experiments, and ultrasonic impact strengthening experiments were analyzed. The results show that the force value in the ultrasonic impact strengthening process is not only the superposition of the static load and the cyclic dynamic impact load, but indicating a coupling effect. The force of ultrasonic impact strengthening process increased by more than 55% compared to the sum of the static load and the maximum dynamic impact load. Moreover, the deformation strain rate of Ti-6Al-4V under separate cyclic dynamic impact loading was simulated. During the ultrasonic impact strengthening process, the deformation strain rate of Ti-6Al-4V could reach 960 s^{-1}, 1587 s^{-1}, and 2043 s^{-1} when the cyclic impact depths of 5 μm, 10 μm, and 15 μm, respectively. At the same time, the material surface hardening mechanism under the high strain rate cyclic impact loading was analyzed. The hardness of Ti-6Al-4V after the ultrasonic impact-strengthening process increased by more than 11% compared to the original hardness. At last, the strengthening performance of Ti-6Al-4V after the ultrasonic impact strengthening was evaluated. The strengthening mechanisms of static and dynamic loads during the ultrasonic impact strengthening of Ti-6Al-4V was investigated.

Keywords Dynamic impact load · Coupling effect · Ultrasonic impact-strengthening · Strain rate · Hardening mechanism

✉ Xuming Zha
  xmzha@jmu.edu.cn

✉ Feng Jiang
  jiangfeng@hqu.edu.cn

1 College of Marine Equipment and Mechanical Engineering, Jimei University, Xiamen 361021, China

2 State Key Laboratory of Digital Manufacturing Equipment and Technology, Huazhong University of Science and Technology, Wuhan 430074, China

3 School of Mechanical, Materials, Mechatronic and Biomedical Engineering, University of Wollongong, Wollongong, NSW 2522, Australia

4 Institute of Manufacturing Engineering, Huaqiao University, Xiamen 361021, China

1 Introduction

As the aerospace industry continues growing, the demands on critical components have increased trend, allowing them to meet ultra-long service times in demanding service environments. Aircraft engines are an essential fundamental support for the development of the aircraft industry. The aero-engine blade is one of the crucial building blocks of the high-performance aero-engine. This blade is subjected to long-time alternating load [1], high temperature and pressure [2], and foreign body impingement [3]. This results in different levels of damage to the blade surface, leading to premature failure of the blades, bringing a substantial potential danger to flight safety. Consequently, it is very important to possess the excellent heat resistance, fatigue resistance, and lightweight performance of the aero-engine blades.

As shown in Fig. 1, titanium alloys are widely used in the aerospace industry due to their low density, high specific strength, good corrosion resistance, and excellent thermal stability. However, titanium alloys have relatively low shear strength and work hardening coefficients [4], as well as high ductility and chemical activity [5]. The surface of the titanium alloy will form a thin oxide layer during the rubbing process which is easily damaged by shear under the action of external forces [6], resulting in relatively poor friction wear performance of the titanium alloy surface. Research shows that a compressive residual stress field which produced by using the surface strengthening technology could effectively improve the wear and fatigue properties of the titanium alloys [7].

Currently, surface-strengthening technology is used to improve blade surface properties, such as shot peening [8], ultrasonic impact strengthening [9], laser impact strengthening [10], ultrasonic peening drilling [11], ultrasonic vibration-assisted micro-grinding [12–14], nitriding [15], and carburizing [16]. With the development of surface-strengthening technologies, the range of applications for traditional aerospace materials has been dramatically expanded. The use of ultrasonic surface modification as a new surface treatment technology, with the advantages of simple, pollution-free, high-efficiency equipment, has been used extensively in the post-processing of steel [17], titanium [18], aluminum [19], and other materials [20–24]. Ultrasonic impact strengthening technology is a coupled process in which a static load is first applied to the surface of the material followed by a high-frequency cyclic dynamic impact load. The indenter tip exerted a specific static force on the surface of the workpiece to ensure close contact between the indenter tip and the material surface. Researchers took advantage of the cold work effect of metals at room temperature [25] to carry out plastic deformation on the metal surface [26] and refine the surface grain [27, 28]. Based on Hall-Petch theory [29],
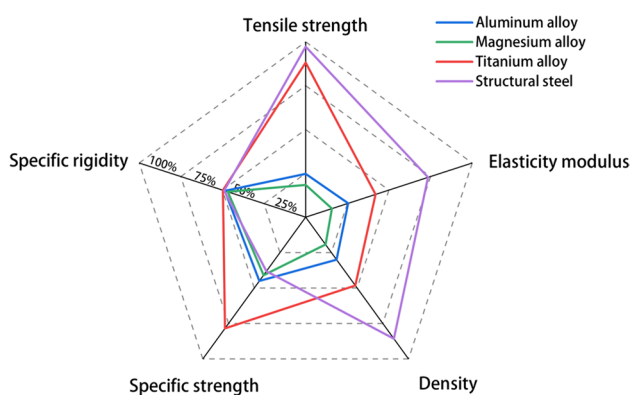
grain refinement caused an increase in the strength of the material thus achieving a strengthening effect, and there was no delamination between the surface of the material strengthening layer and the substrate. Meanwhile, two different deformation mechanisms existed for materials in the ultrasonic impact-strengthening process. The mechanism of the effect of static loading on the material could be explained by the elastic-plastic strain hardening model [30]. However, the effects of dynamic impact loading on materials were based on the intrinsic material model [31] (including strain hardening, strain rate hardening, and thermal softening models) to explain the mechanism of action. As a result, the effect of experimental parameters on material properties during ultrasonic impact-strengthening varies significantly depending on the loading method.

The finite element simulation study of the ultrasonic impact-strengthening saves a great deal of cost and can show the evolution of the contact effect during the ultrasonic impact-strengthening processing more intuitively. Zhang et al. [32] simulated the ultrasonic surface rolling of Al6061-T6 aluminum alloy through modeling to study the effect of process parameters on the residual stress distribution. The dynamic force was much greater than the static force during the ultrasonic surface rolling process. Liu et al. [33] used a finite element model to investigate the effect of different parameters during ultrasonic rolling processing and concluded that the static load plays a more significant role than the dynamic impact. Khan et al. [34] also concluded by constructing a finite element model of the ultrasonic surface nanocrystal modification that a higher static force and smaller impact magnitude could generate residual stresses in the surface and subsurface. Most of the tests performed in the described investigations studied the total contact loading effect during the ultrasonic impact-strengthening process. However, the ultrasonic impact-strengthening process is a coupled effect of the static force and cyclic dynamic impact force. This static force and cyclic dynamic impact force represented different loading methods. Thus, this study used an experiment platform to disassemble the ultrasonic impact-strengthening process into different loading methods. The changes in force values were monitored in real-time during the experiment and used to investigate the coupling process of the static load and cyclic dynamic impact load. Furthermore, the surface morphology and hardness of Ti-6Al-4V were examined to obtain the effects of the different loading methods Ti-6Al-4V. The deformation strain rate of the Ti-6Al-4V subjected to cyclic dynamic impact loading was also derived through simulation modeling to analyze the material hardening mechanism under the action of the high strain rate impact. The above analysis could provide technical support for optimizing the process parameters of the ultrasonic impact-strengthening of Ti-6Al-4V.

Fig. 1 The specific mechanical properties of different materials

Table 1 The specific mechanical properties of Ti-6Al-4V

Yield strength (GPa)	Tensile strength (MPa)	Shear strength (MPa)	Elongation	Section shrinkage	Modulus of elasticity (GPa)	Density (kg/m^3)
1.098	941	550	14%	46%	113	4430

2 Material and experimental methods

2.1 Material of workpiece

The workpiece material used in this experiment was Ti-6Al-4V. The specific mechanical properties of Ti-6Al-4V are shown in Table 1. The chemical composition of Ti-6Al-4V is shown in Table 2. Due to the high specific strength of titanium, it is widely used in the aerospace field. In this study, the specimen was wire-cut into a square specimen of 8 mm × 8 mm × 3 mm. After the wire cut, the specimens were placed in the cold inlay mold, and the configured epoxy resin was poured into the mold. Then the solidified specimen was polished. The mesh number of sandpaper was 60 #, 500 #, 1500 #, 2000 #, and 4000 #. The surface morphology of Ti-6Al-4V before and after polishing is shown in Fig. 2. The polishing time increased with the increasing mesh number of sandpaper. The scratch on the specimen surface was eliminated through microscope observation, meeting the requirements of the metallographic preparation.

2.2 Ultrasonic impact-strengthening experiment platform

The overall structure of the ultrasonic impact-strengthening experiment platform is shown in Fig. 3. Comprising a motion module, an ultrasonic impact system module and a data acquisition module. Compared with other devices, this equipment can achieve high-precision displacement control

Table 2 Chemical composition of the Ti-6Al-4V

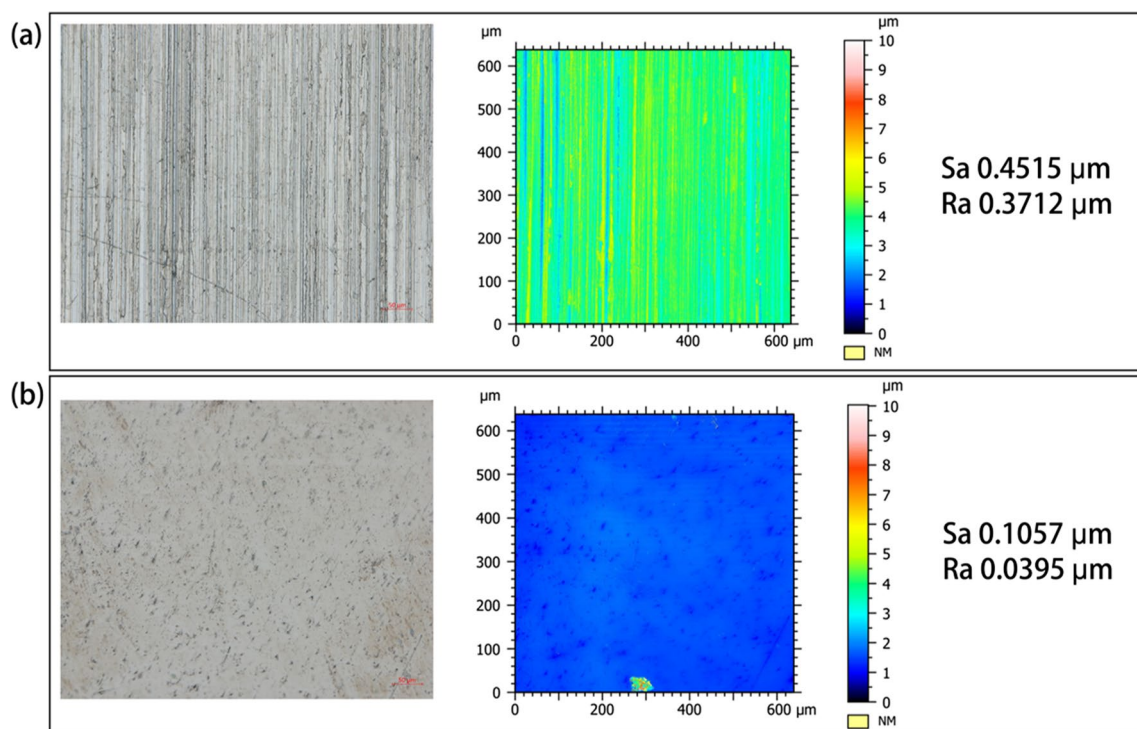| Al	V	Fe	C	N	H	O	Ti
6.09%	4.06%	0.03%	0.014%	0.013%	0.001%	0.14%	Balance

Fig. 2 The surface morphology of Ti-6Al-4V before polishing (**a**) and after polishing (**b**)
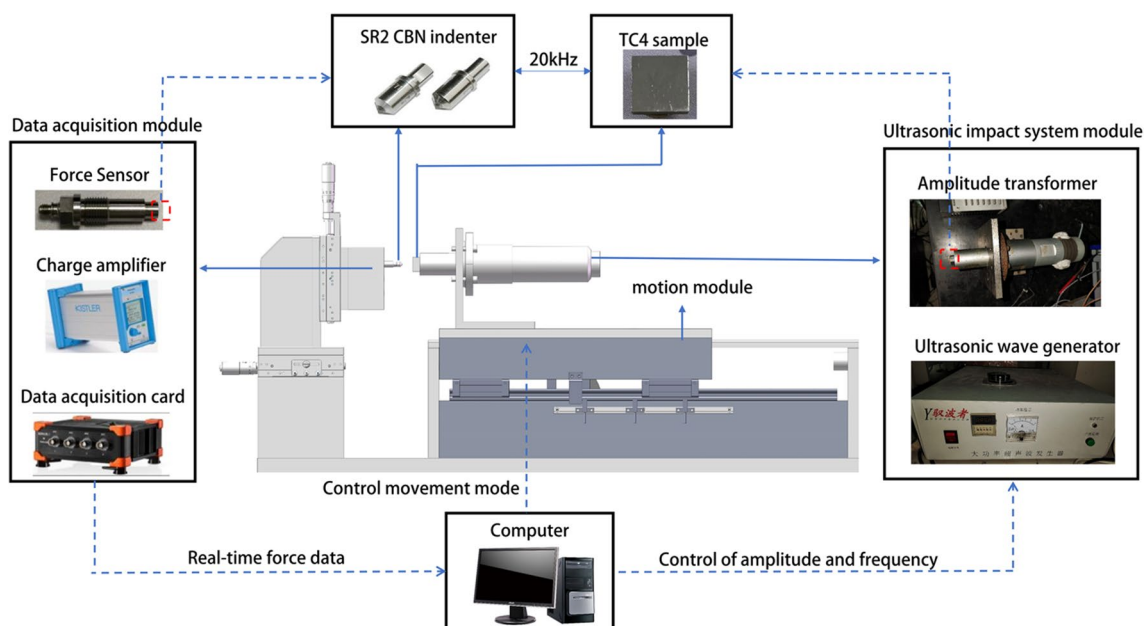
Fig. 3 The overall structure of an ultrasonic impact-strengthening experiment platform

of the indenter tip and monitor the value of the real-time impact force during the impact process.

The motion module could withstand a transverse rated load of 1500 N and a maximum transverse load of 3000 N. At the same time, it could move at a speed of 2 m/s. With the help of the Renishaw RG2 linear encoder system, the movement of the specimen relative to the indenter was monitored. In addition, the repetitive positioning accuracy of the linear drive could reach 0.5 μm through the Renishaw Close-loop System. During this process, the indenter tip was mounted on an XY table, and the impact position was adjusted as required [35].

The ultrasonic-impact module includes an indenter, an amplitude transformer, and an ultrasonic wave generator. First, the material of the indenter is CBN, with a radius of 2 mm. The second part, an ultrasonic-wave generator, could control the impact amplitude and time between the indenter tip and the specimen surface. Furthermore, it could continuously transmit a sinusoidal signal with a frequency of 20 kHz. After that, the amplitude transformer could convert the 20 kHz sine-wave signal into mechanical energy [36], causing the indenter tip to apply a periodic dynamic load to the specimen surface. Meanwhile, the indenter tip was connected to a force sensor. A data acquisition module was applied to measure the dynamic load signal in real-time during the impact process between the indenter tip and the material surface. Based on the piezoelectric measurement principle, dynamic force data were measured using a high-sensitivity force sensor (Kistler 9203) with a high natural frequency of 27 kHz. The sampling results were imported into the DEWESoftX2 for data analysis through the charge amplifier (Kistler 5080A) and data acquisition board (5697A1 DAQ system) [37–39]. During the measurement process, the sampling frequency of the data acquisition board was set as 100 kHz. Besides, the data acquisition module performed an interpolation algorithm based on the measured data.

2.3 Experimental method for disassembling the ultrasonic impact process

This study decomposed the ultrasonic impact-strengthening process into three experiments through the experiment platform to investigate the strengthening mechanism of Ti-6Al-4V, including (1) static load experiment, (2) high-frequency cyclic dynamic impact experiment, and (3) ultrasonic impact-strengthening experiment. The experimental parameters are summarized in Table 3. In this study, each experiment was performed three times to reduce errors.

The schematic diagram of the static load experiment is shown in Fig. 4a. In this section, the linear motor motion

Table 3 Experimental protocol for decomposition of ultrasonic impact processes

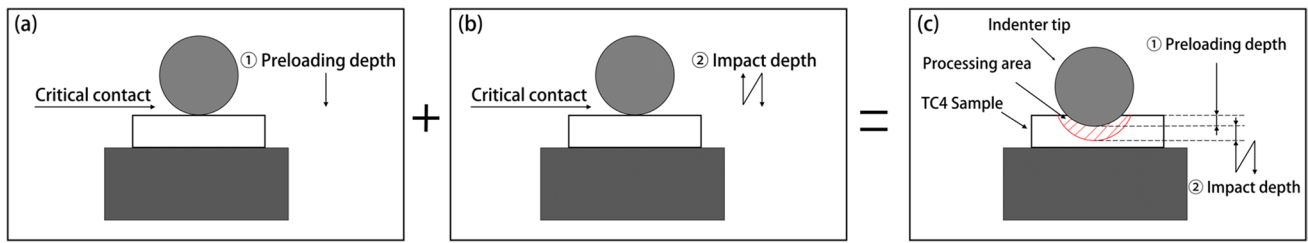| Preloading depth (μm)	Impact depth (μm)	Total depth (μm)
5	5	5+5
10	10	10+10
15	15	15+15

Fig. 4 Disassembly of the ultrasonic impact-strengthening process: **a** static load experiment, **b** high-frequency cyclic dynamic impact experiment, **c** ultrasonic impact-strengthening experiment

was controlled by the computer to make critical contact between the indenter tip and Ti-6Al-4V. At this moment, the force measuring instrument measured the contact load between the indenter tip and the specimen at 0.01 N. After that, a controlled indenter tip was pressed into the surface of Ti-6Al-4V at a constant speed of 1 mm/s. The magnitude of the static load was controlled by displacing the indenter into the surface of Ti-6Al-4V.

The description of the high-frequency cyclic dynamic impact experiments is shown in Fig. 4b. The linear motor motion is controlled by the computer to make critical contact between the indenter tip and Ti-6Al-4V. At first, the force measuring instrument measured the contact load between the indenter tip and the specimen at 0.01 N. Next, the ultrasonic wave generator continues outputting a sine-wave signal at a frequency of 20 kHz, causing the indenter tip to apply a periodic cyclic dynamic load to the specimen surface. In this process, the magnitude of the cyclic dynamic impact load was controlled by the amplitude provided by the ultrasonic wave generator.

The schematic diagram of the ultrasonic impact-strengthening experiment is shown in Fig. 4c. In detail, the surface of the Ti-6Al-4V was preloaded by controlling the indenter tip pressing in with a constant speed of 1 mm/s. Next, the magnitude of the preload was controlled by the press-in displacement. Then, the ultrasonic wave generator continued outputting a sine-wave signal at a frequency of 20 kHz, resulting in the indenter tip applying a periodic cyclic dynamic load to the surface of the specimen. In the meantime, the coupled forces of the static load and the cyclic dynamic impact load were applied to the surface of Ti-6Al-4V.

2.4 Surface morphology characterization

Craters formed on the surface of Ti-6Al-4V after the static load experiment, high-frequency cyclic dynamic impact experiment, and the ultrasonic impact strengthening experiment. The three-dimensional profile of the crater region was measured through a Zeiss laser confocal microscope (LSM900) to obtain the depth and width of the crater. The surface morphology of the craters was examined through a

Zeiss scanning electron microscope (Crossbeam 550). Under different experimental parameters, the plastic flow and the crack extension within the surface cater of the Ti-6Al-4V were observed.

2.5 Hardness characterization

The surface Vickers' hardness of Ti-6Al-4V after experiments was measured by the Ultra-micro-Hardness Tester (DUH-211, SHIMADZU). A square-based diamond pyramid indenter with an included angle of 136° between opposing faces, a maximum load of 1961 mN, a loading time of 10 s was applied during the hardness testing. Figure 5 shows the schematic diagram of the hardness test, and each tested value is the average of nine data points.

2.6 Finite element modeling

As a dynamic loading process, the coupling of static force and cyclic dynamic impact force in the ultrasonic impact-strengthening could cause the indenter tip to obtain high instantaneous velocity and acceleration. This could lead to a high strain rate which might evoke material embrittlement in the machining process [40, 41]. As a strain-rate sensitive material, the mechanical properties of Ti-6Al-4V changed under the high strain-rate impact. Therefore, it is essential to obtain the deformation strain rate of
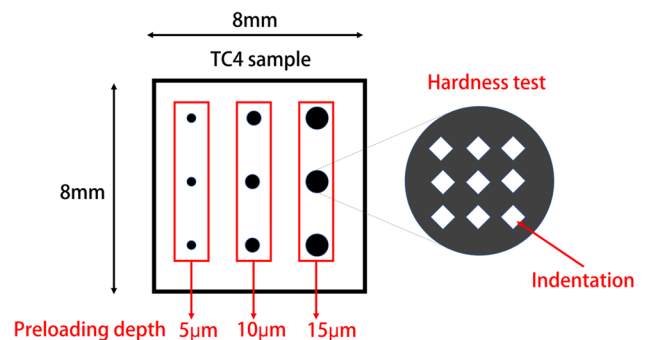

Fig. 5 Schematic diagram of hardness testing

Ti-6Al-4V during the dynamic loading. In this process, a three-dimensional ultrasonic impact process simulation model was established through the finite element software ABAQUS. The cyclic dynamic impact force values and plastic deformation strain rates of Ti-6Al-4V could be obtained through the simulation of the high-frequency cyclic dynamic impact experiment.

The ultrasonic impact process model and mesh division are shown in Fig. 6. The model size of Ti-6Al-4V was 8 mm × 8 mm × 3 mm, and the indenter tip was a sphere with the diameter of 4 mm. Due to the accuracy of the calculation results, researchers reduced the solution time and improved the calculation efficiency. Through ABAQUS finite element software, the mesh size of the impact region was refined to 0.05 mm. All meshes applied 8-node hexahedral linear to reduce integral cells with 271,680 cells and 284,846 nodes. The indenter tip was defined as a nondeformable rigid body due to its hardness and strength were much higher than Ti-6Al-4V. A generic contact type was applied between the indenter tip and Ti-6Al-4V with a penalty function contact algorithm. Meanwhile, the penalty friction coefficient μ = 0.1 was selected. Furthermore, the bottom surface of Ti-6Al-4V was fixed entirely, while the load was applied to the reference point set in the center of the sphere.

Tables 4 and 5 show the basic parameters of Ti-6Al-4V and CBN. During the ultrasonic impact process, the material surface was subjected to static forces and high-frequency cyclic impact forces exerted by the indenter tip, resulting in plastic deformation. The yield strength of the material changed with the strain rate. Since the Johnson-Cook constitutive model could describe the plastic mechanical properties of the material during the ultrasonic impact process, it was selected as the material constitutive model. Furthermore, the material yield limit formula [42] is shown in Eq. (1):
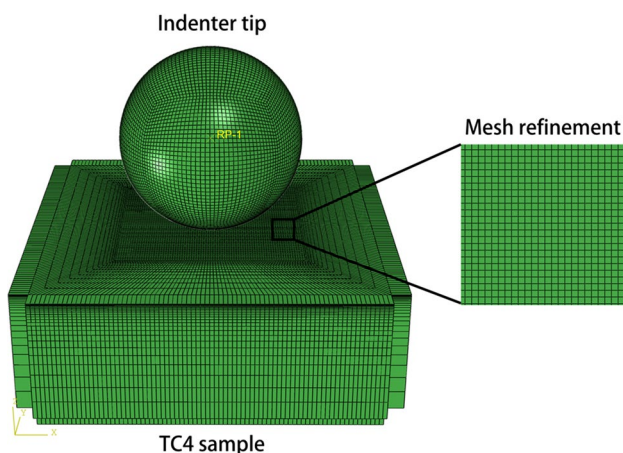

Fig. 6 Finite element model of the ultrasonic impact process

Table 4 Ti-6Al-4V material properties [43]

Density (kg/m^3)	Modulus of elasticity (GPa)	Poisson's ratio	Yield strength (GPa)
4430	113	0.342	1.098

$$\delta = (A + B\varepsilon^n)(1 + Cln\dot{\varepsilon}^*)(1 - T^{*m}) \tag{1}$$

In the formula, A is the yield strength, B is the strain hardening parameter, C is the empirical strain rate sensitivity coefficient, n is the hardening rate, ε is the plastic strain rate, T^* is the temperature influence factor, m is the temperature sensitivity coefficient, and $\dot{\varepsilon}^*$ is the strain influence factor. The intrinsic structural parameters of Ti-6Al-4V are shown in Table 6.

3 Result and discussion

3.1 Force analysis

3.1.1 Force analysis during the static load experiment

The real-time force values for press-in displacements at 5 μm, 10 μm, and 15 μm during the static load experiment are shown in Fig. 7. The force could reach 3.44 N, 6.84 N, and 10.54 N when the indenter tip pressing into 5 μm, 10 μm, and 15 μm of the Ti-6Al-4V surface, respectively. In addition, it could be concluded that the static force measured during the experiments had a positive relationship with the preloading depth of the indenter tip.

3.1.2 Force analysis during the dynamic impact experiment

The impact force measured at different cyclic dynamic impact depths are shown in Fig. 8. The impact process is divided into three phases: (1) critical contact, (2) initial impact, (3) stable impact. During the initial impact phase, the surface of Ti-6Al-4V was suffered elastic-plastic deformation. The measured dynamic force value reached the largest when the indenter tip pressed into the surface of Ti-6Al-4V with the deepest distance. Subsequently, elastic recovery occurred on the surface of Ti-6Al-4V, and the plastic deformation was permanently retained. After that, the impact process entered into the stable impact phase. It was clear that the cyclic dynamic impact force values increased with raising the impact depth. The

Table 5 CBN material properties [44]

Density(kg/m^3)	Modulus of elasticity (GPa)	Poisson's ratio
11900	534	0.22

Table 6 Ti-6Al-4V constitutive model parameters [42]

A/yield strength (GPa)	B/strain hardening parameter (GPa)	n/hardening rate	m/temperature sensitivity coefficient	Melting temperature (K)	Reference temperature (K)	C/empirical strain rate sensitivity coefficient	$\dot{\varepsilon}^*$/strain influence factor
1.098	1.092	0.93	1.1	1878	298	0.014	1
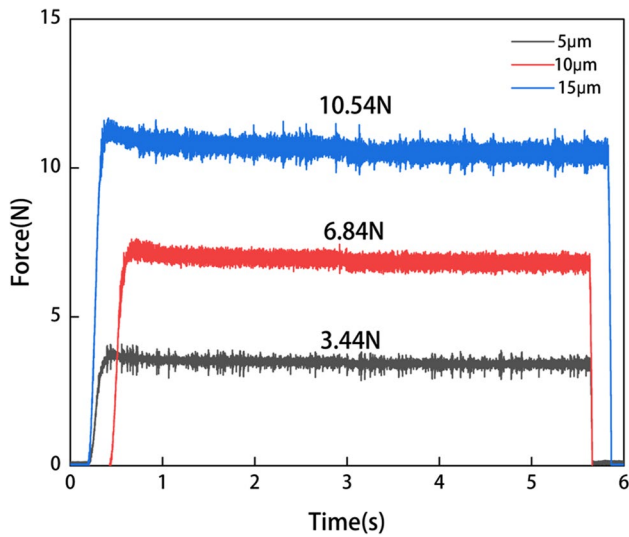
Fig. 7 The magnitude of the static force at different preloading depths

average stable dynamic impact force values for amplitudes at 5 µm, 10 µm, and 15 µm were 9.54 N, 16.31 N, and 21.31 N, respectively. The vibration frequency of the indenter tip was 20 kHz, with one cycle of 5×10^{-5} s. Compared with the static load experiment, the indenter tip could obtain a high acceleration during the loading process in each cycle. Therefore, the cyclic dynamic impact force applied on the surface of Ti-6Al-4V was significantly larger than that of the static force. Furthermore, it could be found that there were negative values of dynamic impact force occurred during the impact process. This could be due to the local thermal field generated by the ultrasonic high-frequency cyclic impact. It induced the thermal softening and bonding effect between the indenter tip and the surface of Ti-6Al-4V. When the indenter tip began to unloading, the bonding effect between the indenter tip and the surface of the Ti-6Al-4V could produce a pulling force in the opposite direction.
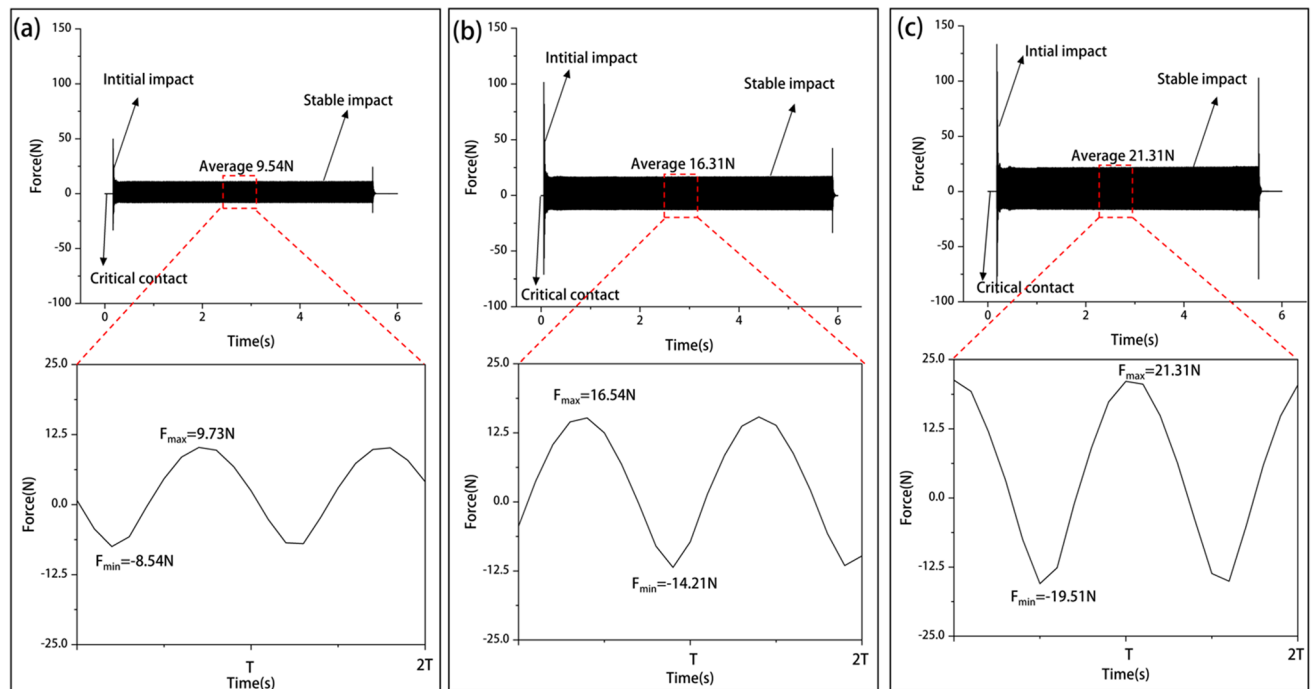

Fig. 8 Impact force values at different amplitude: **a** 5 µm impact depth; **b** 10 µm impact depth; **c** 15 µm impact depth
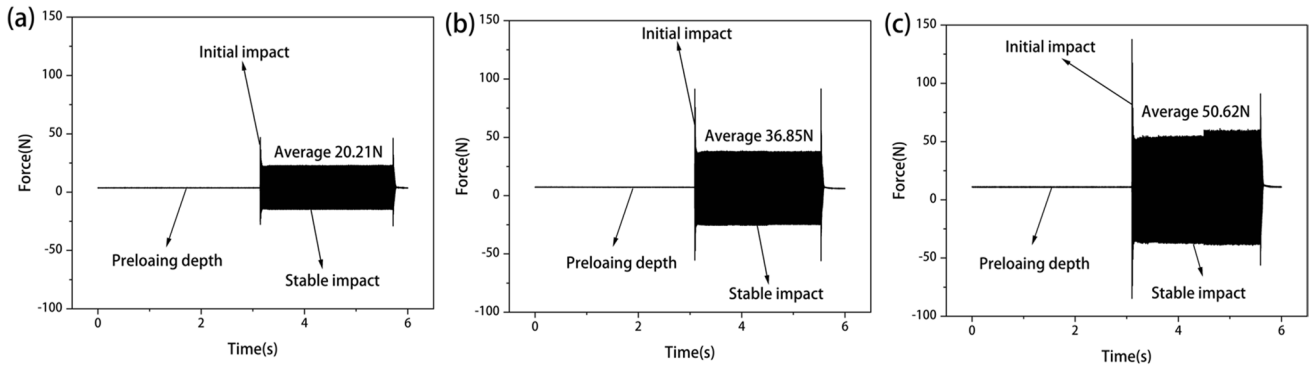
Fig. 9 Analysis of ultrasonic impact strengthening force values under different parameters: **a** 5 μm preloading depth + 5 μm impact depth; **b** 10 μm preloading depth + 10 μm impact depth; **c** 15 μm preloading depth + 15 μm impact depth

3.1.3 Force analysis during the ultrasonic impact strengthening experiment

The measured force-time relationship during the ultrasonic impact strengthening process is shown in Fig. 9. This entire process is divided into two stages. The first stage was the preloading applied on the surface of Ti-6Al-4V, representing the static load application. The second stage is the coupling of the cyclic dynamic impact load based on the static load. The force values in the initial and stable impact phases during the ultrasonic impact experiments had similar trends to the high-frequency cyclic dynamic impact experiment. Meanwhile, the average values of the stable impact phase for 5 μm impact depth based on 5 μm preload depth (5 μm

preload depth + 5 μm impact depth), 10 μm impact depth based on 10 μm preload depth (10 μm preload depth + 10 μm impact depth), and 15 μm impact depth based on 15 μm preload depth (15 μm preload depth + 15 μm impact depth) were 20.21 N, 36.85 N, and 50.62 N, respectively.

Figure 10 shows the function fit plot of the stable impact stage of the 5 μm preloading depth + 5 μm impact depth, 10 μm preloading depth + 10 μm impact depth, 15 μm preloading depth + 15 μm impact depth. As shown in Fig. 10a, the static load was always kept at 3.44 N when the preloading depth and impact depth were 5μm. The dynamic impact load is fitted to the average impact force values during the stabilization phase of Fig. 8. After calculated, the cyclic dynamic force is a sinusoidal act of periodic variation from − 9.56 to 9.56 N.

Fig. 10 Function fitting diagram of the stable impact stage: **a** 5 μm preloading depth + 5 μm impact depth; **b** 10 μm preloading depth + 10 μm impact depth; **c** 15 μm preloading depth + 15 μm impact depth; **d** force value statistic chart
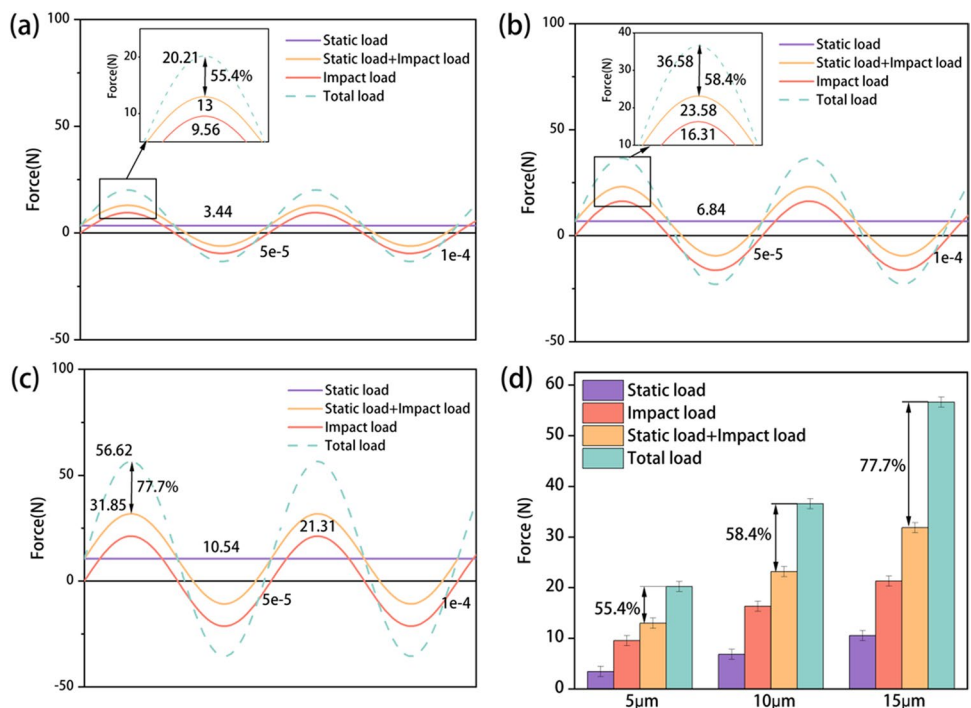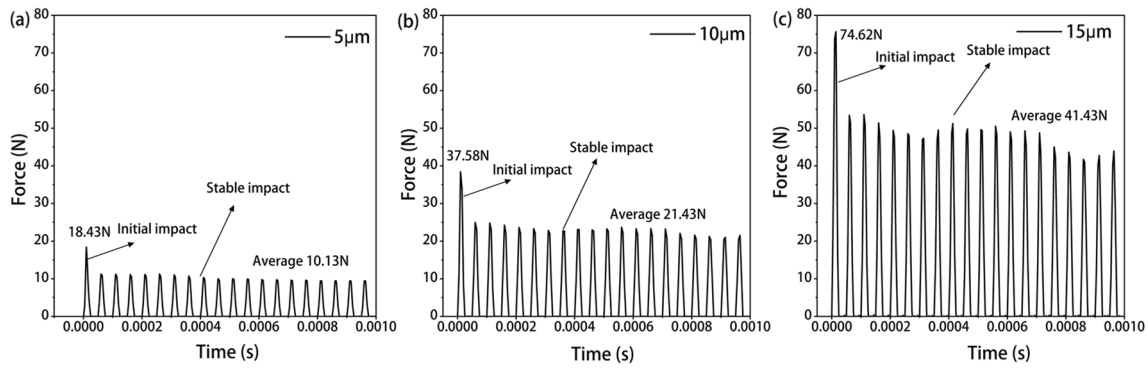
Fig. 11 Force values for different impact depths in the cyclic dynamic impact simulation model: **a** impact depth of 5 μm; **b** impact depth of 10 μm; **c** impact depth of 15 μm

Meanwhile, the total load and the impact load are act of sinusoidal character with the common frequency in the defined period. The maximum value of the total force is 20.21 N. The sum of the static load and the maximum dynamic impact load is only 13 N. In contrast, the force value has improved up about 55.4%. As shown in Fig. 10b, the static load was always kept at 6.84 N when the preloading depth and impact depth were 10 μm. The cyclic dynamic force is a sinusoidal act of periodic variation from − 16.31 to 16.31 N. The maximum value of the total force is 36.58 N. However, the sum of the static load and the maximum dynamic impact load is only 23.85 N. In contrast, the force value has improved up about 58.4%. As shown in Fig. 10c, the static load was always kept at 10.54 N when the preloading depth and impact depth were 15 μm. The cyclic dynamic force is a sinusoidal act of periodic variation from − 21.31 to 21.31 N. The maximum value of the total force is 56.62 N. The sum of the static load and the maximum dynamic impact load is only 31.85 N. In comparison, the force value has improved up about 77.7%. Figure 10 d shows the static and impact load force values for these three groups with different parameters of the ultrasonic impact strengthening experiments. Based on the results, the force value in the ultrasonic impact strengthening process is not only the superposition of the static load and the cyclic impact load, but indicating a coupling effect. The degree of coupling effect becomes more obvious under the condition of the deeper press-in depth and the larger impact amplitude.

3.1.4 Simulation analysis of the force during dynamic impact experiments

The impact force values derived from this simulation model for the ideal case were compared with the actual impact force values to verify the validity of the simulation model. The force values of the cyclic dynamic impact simulation model at different impact depths are shown in Fig. 11. It could be found that the impact process is divided into two phases: (1) initial impact; (2) stable impact. The trend of the simulated cyclic impact force is almost same as the actual cyclic impact force in the experiments. In each impact cycle, it showed that the impact force increasing to the maximum value, which indicated the indenter tip continued pressing into the material surface. Then, the impact force decreasing to the minimum value, which implied that the indenter tip moved out of the material surface. Table 7 shows the cyclic dynamic impact force error between the simulation and experiments. At the impact amplitude of 5 μm, 10 μm, and 15 μm, the force error between the simulation and experiment in the stable impact phase was approximately 5%, 30%, and 93%, respectively. It showed that the calculation error will be increasing as the impact amplitude improved. This could be due to the thermophysical properties of Ti-6Al-4V affects the accuracy of the simulation results. During the cyclic dynamic impact experiment, the high-frequency cyclic impact and intense friction between the indenter tip and the surface of Ti-6Al-4V created a local thermal field. This could cause the softening of

Table 7 Comparison of simulation and experimental force value error

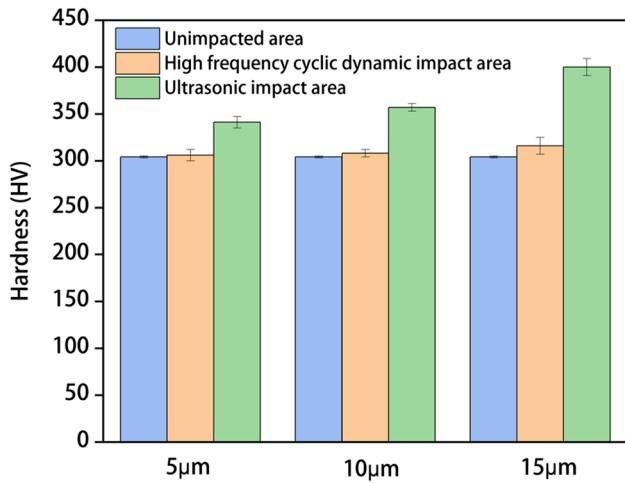| Impact amplitude (μm)	Simulation of initial impact force values (N)	Experimental of initial impact force values (N)	Error	Simulation of stable impact force values (N)	Experimental of stable impact force values (N)	Error
5	18.43	50	63%	10.13	9.64	5%
10	37.58	99.17	62%	21.43	16.31	30%
15	74.62	136.4	45%	41.43	21.31	93%

Fig. 12 Comparison of the hardness of Ti-6Al-4V under different loading experiments

the surface of Ti-6Al-4V and induce the impact force decreased in the actual experiments.

3.2 Hardness

The hardness of Ti-6Al-4V after the high-frequency cyclic dynamic impact experiments and the ultrasonic impact-strengthening experiments is shown in Fig. 12. It could be

found that the hardness of Ti-6Al-4V has increased by 0.6%, 1.3%, and 3.9% compared to the original hardness after the high-frequency cyclic dynamic impact experiments with the impact depth of 5 µm, 10 µm, and 15 µm, respectively. The hardness of Ti-6Al-4V has increased by 11.2%, 15.6%, and 26.5% compared to the original hardness after the ultrasonic impact strengthening experiments with the impact depth based on preload depth of 5 µm, 10 µm, and 15 µm, respectively. In short, it could be concluded that the hardness of Ti-6Al-4V has a considerable increase after the ultrasonic impact-strengthening experiments.

3.3 Strain rate

The performance evolution of material responses to the high strain-rate during the ultrasonic impact-strengthening process is very important. The evolution process of strain rate of the impact depth of 5 µm, 10 µm, and 15 µm at the center of the contact area obtained from the simulation model during the high-frequency cyclic dynamic impact experiment is shown in Fig. 13. Table 8 shows the strain rate value of the cyclic impact depth of 5 µm, 10 µm, and 15 µm which obtained from the simulation during the high-frequency cyclic dynamic impact experiment. In the initial phase of the cyclic dynamic impact depth of 5 µm, the surface of Ti-6Al-4V was subjected to the high impact force which induced the strain
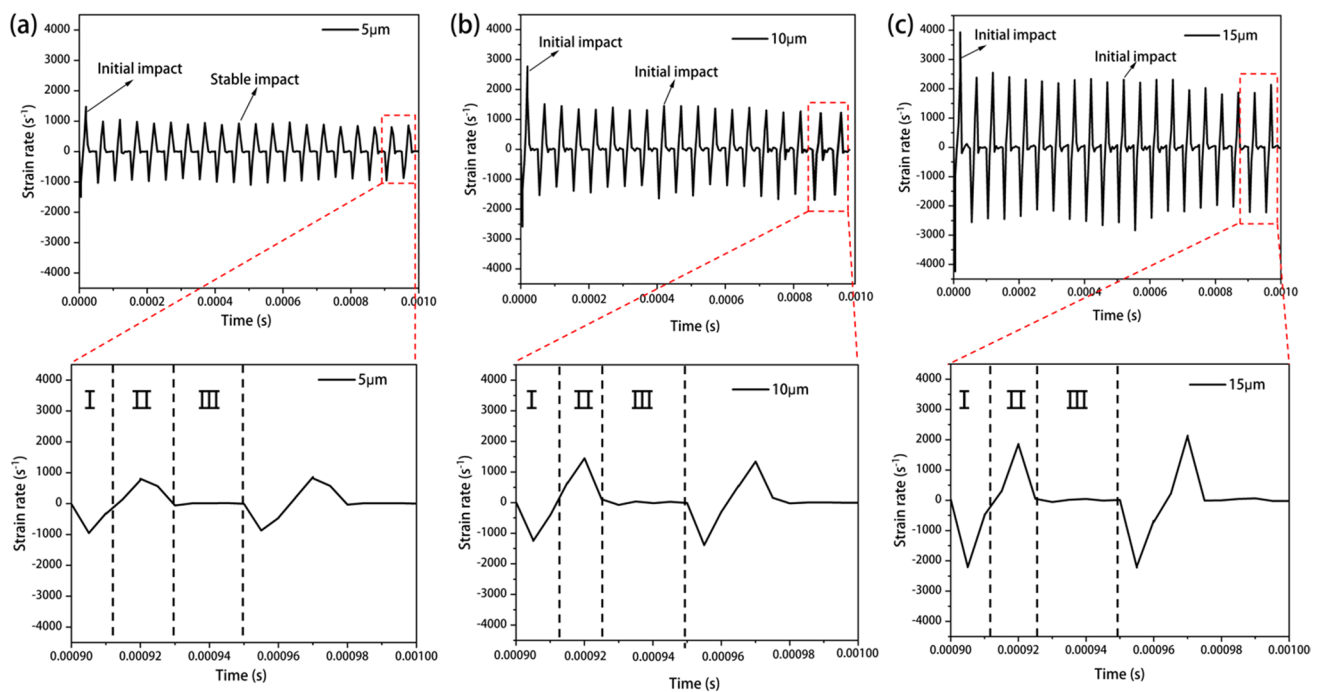

Fig. 13 Strain rate of the material surface under different cyclic impact depths: **a** trend of strain rate at 5 µm cyclic impact depth over time in 0.001 s; **b** trend of strain rate at 10 µm cyclic impact depth

over time in 0.001 s; **c** trend of strain rate at 15 µm cyclic impact depth over time in 0.001 s

Table 8 Plastic deformation strain rate of the material surface under different cyclic impact depths

Amplitude (μm)	5	10	15
Initial strain rate (s^{-1})	1564	2792	3969
Stable strain rate (s^{-1})	960	1587	2043

rate up to 1564 s^{-1}. Then, during the stable phase of the cyclic dynamic impact depth of 5 μm, the average strain rate was about 960 s^{-1}. As the cyclic dynamic impact depth reached to 10 μm, the strain rate on the surface of Ti-6Al-4V in the initial phase and stable phase was 2792 s^{-1} and 1587 s^{-1}, respectively. When the cyclic impact depth continued increasing to 15 μm, the strain rate on the surface of Ti-6Al-4V in the initial phase and stable phase was 3969 s^{-1} and 2043 s^{-1}, respectively. Therefore, there is a positive correlation between the cyclic impact depth and plastic deformation strain rate of Ti-6Al-4V. In addition, it could be found that the stable phase was divided into three stages by amplifying the impact process of two cycles. Stage 1: the indenter tip pressed into the surface of Ti-6Al-4V rapidly, and the surface was compressed and deformed rapidly due to the impact loading. Stage 2: the indenter tip moved in the opposite direction while the surface of Ti-6Al-4V occurred elastic recovery during the unloading. Stage 3: the indenter tip was detached from the surface of Ti-6Al-4V entirely.

As shown in Fig. 14, the yield strength of the material raised with increasing the strain rate. The correlation between the yield strength and the strain rate [45] is shown in Eq. (2):

$$\sigma = f(\varepsilon, \dot{\varepsilon}, T) \tag{2}$$

In the formula, σ is the yield strength, ε is the material strain, $\dot{\varepsilon}$ is the strain rate, and T is the temperature. The toughness of the material K_f [46] is shown in Eq. (3). The brittleness of the material B [40] can be expressed in Eq. (4):

$$K_f = \int_0^{\varepsilon_f} f(\varepsilon, \dot{\varepsilon}, T)d\varepsilon \tag{3}$$

$$B = \frac{\sigma}{k_f} \tag{4}$$

In the formula, ε_f is the fracture strain. As the yield strength increased, the toughness of the material decreased, and the brittleness of the material increased. The relationship between the hardness and yield strength [47] is shown in Eq. (5):

$$HV = 3A\sigma(0.1)^{-n} \tag{5}$$

In the formula, HV is the hardness of the material, A is the influence factor 1.12, σ is the yield strength, and n is the work-hardening index. It could be concluded that the hardness of the material raised with increasing the yield strength.

The dynamic impact loading induced the high velocities and accelerations. This could increase the plastic deformation strain rate of Ti-6Al-4V and lead to the material embrittlement [40]. Moreover, it can be inferred that when the dynamic impact loading applied base on a static loading, this static preload is conducive to the energy transmission between the tool and material during the ultrasonic impact-strengthening

Fig. 14 Schematic diagram describing the effect of strain rate on strength and toughness of a material [40]
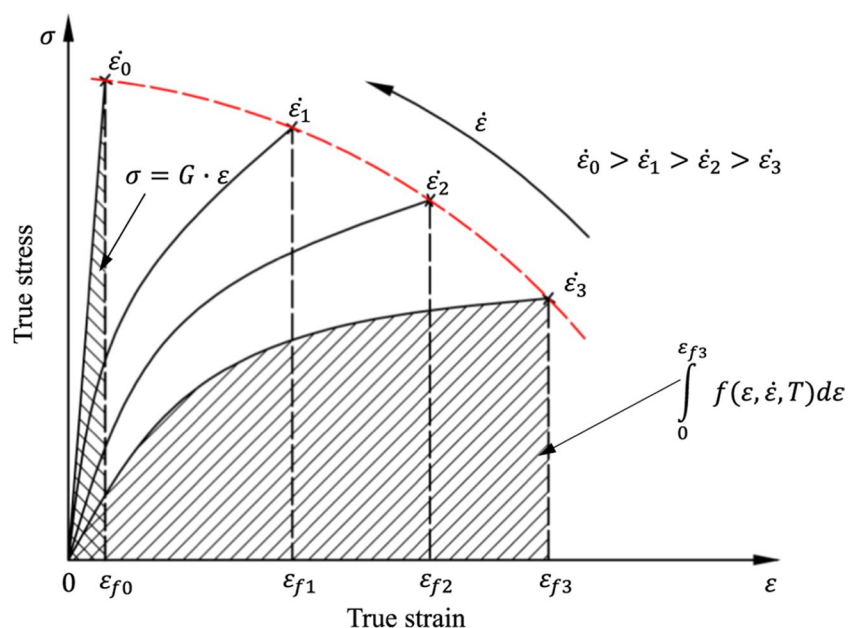
process. It could cause a larger plastic deformation strain rate and material embrittlement effect. In the cyclic dynamic impact experiments, the impact force and strain rate raised with increasing the impact depth. As shown in Fig. 12, the enhance of embrittlement effect might not be significantly under the impact depth of 5 µm and 10 µm. This resulting in an insignificant rise of the surface hardness of Ti-6Al-4V. When the strain rate and embrittlement effect were further increased under the impact depth of 15 µm, there is a significant enhancement effect of the hardness of Ti-6Al-4V. The hardness could be improved about 3.9% compared with the original hardness of Ti-6Al-4V. In the ultrasonic impact-strengthening experiments, the coupling effect of the static loading and the cyclic dynamic impact loading resulted in a larger enhancement of the strain rate and embrittlement effect of Ti-6Al-4V. As shown in Fig. 12, it was observed that the hardness was improved about 11.2%, 15.6%, 26.5% after the experiments of the 5 µm preloading depth + 5 µm impact depth, 10 µm preloading depth + 10 µm impact depth, 15 µm preloading depth + 15 µm impact depth, respectively, which compared with the original hardness of Ti-6Al-4V.

3.4 Surface morphology

3.4.1 Surface morphology analysis after the dynamic impact experiment

Figure 15 shows the residual craters on the surface of Ti-6Al-4V after the cyclic dynamic impact experiments with the impact depth of 5 µm, 10 µm, and 15 µm. It was observed that the width and depth of the residual craters became larger as
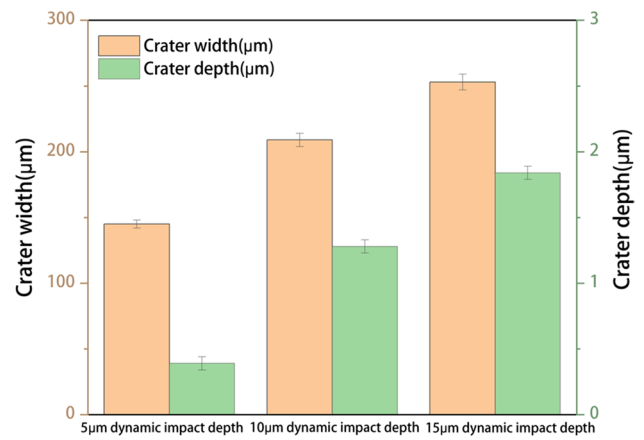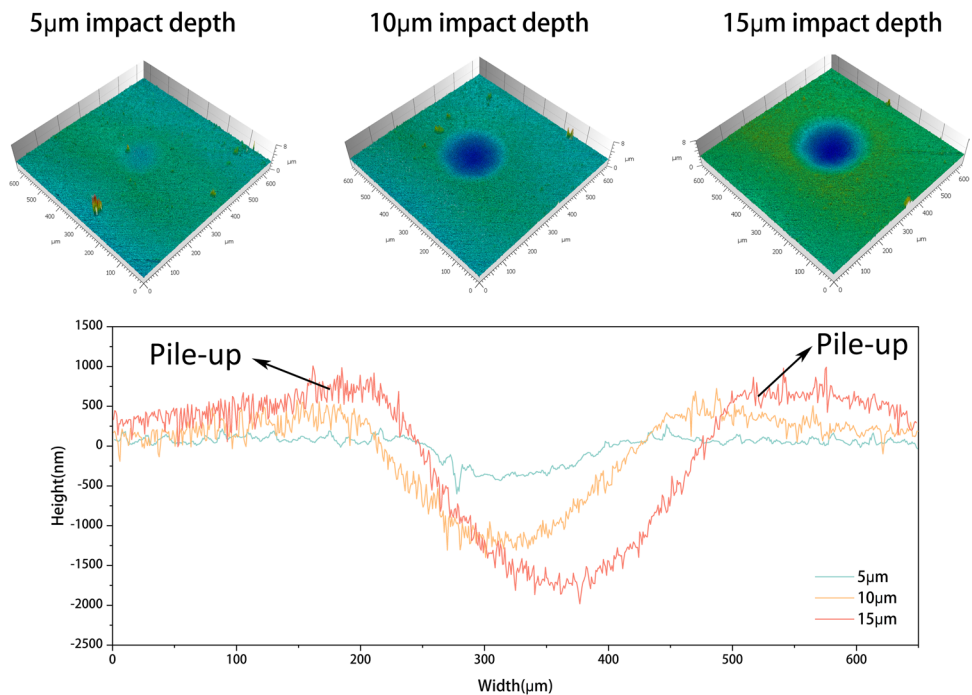

Fig. 16 Width and depth of the residual craters at different impact depths

the impact depth increased. The value of width and depth of the residual craters on the surface of Ti-6Al-4V after different impact depths are shown in Fig. 16. When the impact depth was 5 µm, the width and depth of the crater were about 145 µm and 0.39 µm, respectively. When the impact depth was increased to 10 µm, the width and depth of the crater were about 209 µm and 1.28 µm, respectively. When the impact depth was reached to 15 µm, the width and depth of the crater were about 253 µm and 1.84 µm, respectively. The degree of plastic deformation of Ti-6Al-4V raised with increasing the impact depth. In addition, the plastic flow characteristic of Ti-6Al-4V led to the pile-up of material on both sides of the crater.
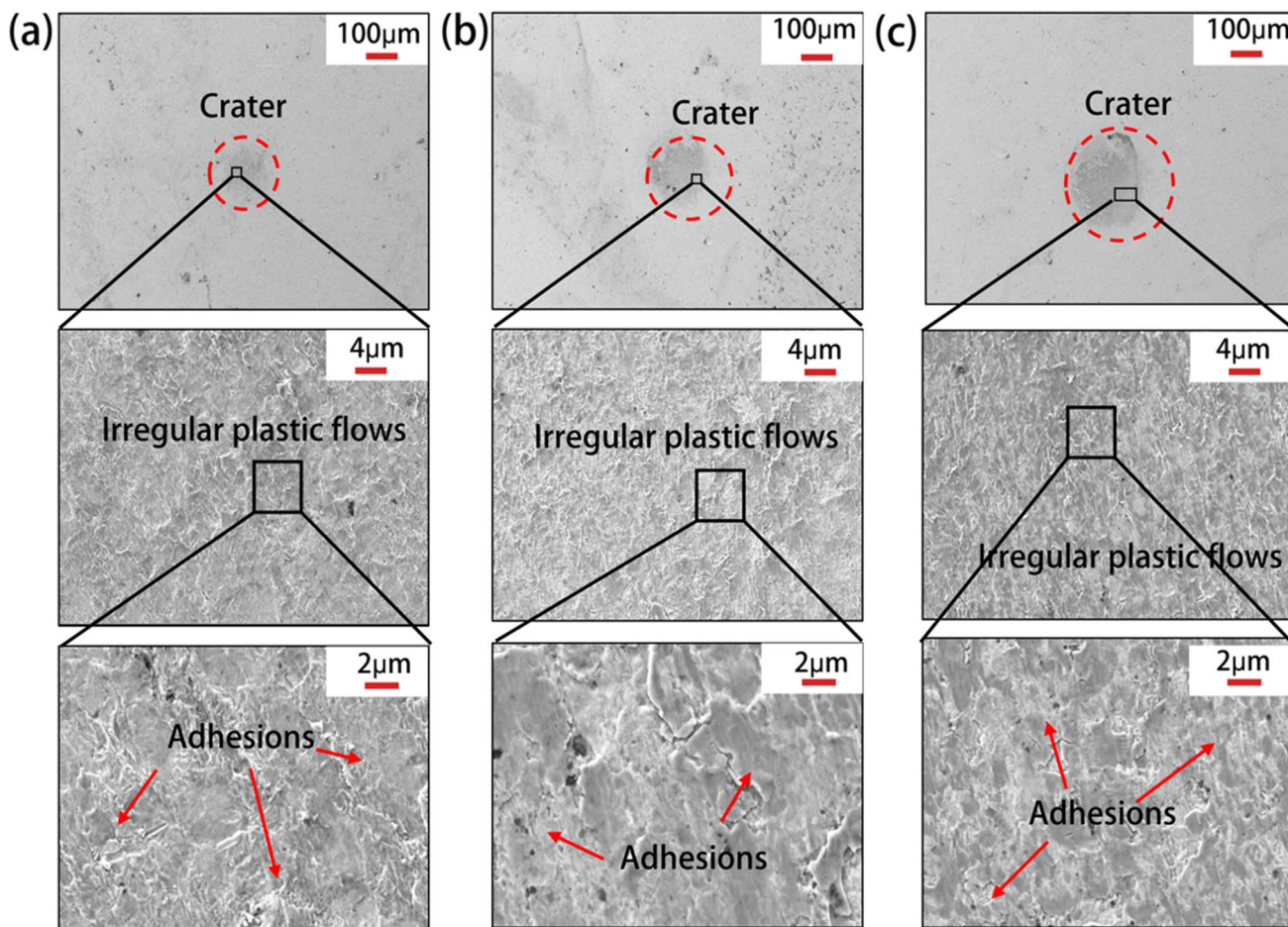
Fig. 15 Surface images and cross-sectional profiles of the craters at different impact depths

Fig. 17 Surface morphology of the craters under different cyclic impact depths: **a** impact depth of 5 μm; **b** impact depth of 10 μm; **c** impact depth of 15 μm

Figure 17 shows the surface morphology of the craters after the high-frequency cyclic dynamic impact experiments with the impact depth of 5 μm, 10 μm, and 15 μm. It found that the characteristic of the irregular plastic flow was appeared inside the craters. Besides, it was observed that some titanium oxides were bonded on the surface of craters from the magnifying morphology. The distribution area of the adhesive material inside the craters was raised significantly with increasing the impact depth. The elemental analysis of the impact region (inside craters) and unimpact region (outside craters) is shown in Fig. 18. The oxygen element content of the contact surface of Ti-6Al-4V was increased from 13.51 to 23.19% after the cyclic dynamic impact experiments. This could be due to the high temperature occurred in the contact area during the high-frequency cyclic

Fig. 18 a Elemental analysis of the impact region and unimpact region; **b** weight percentage of the elemental content
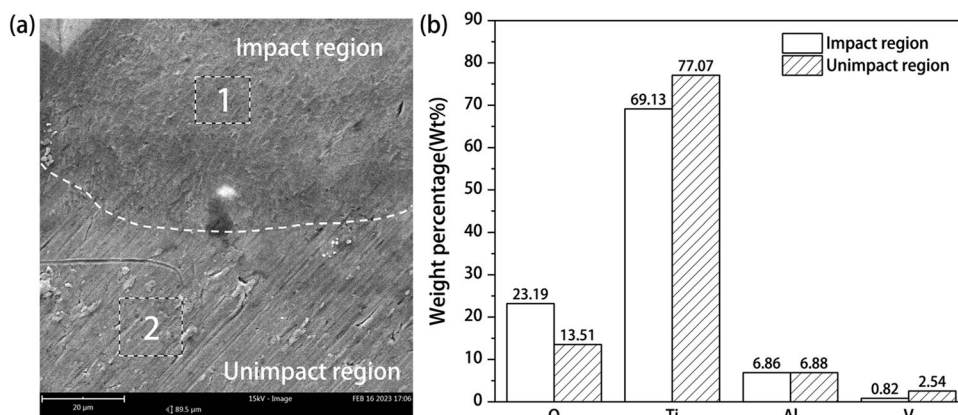
impact process. Under the condition of high temperature and intense friction, the oxidation and adhesion effect of Ti-6Al-4V has emerged gradually, and this action grew more intense.

3.4.2 Surface morphology analysis after the ultrasonic impact strengthening experiment

Figure 19 shows the residual craters on the surface of Ti-6Al-4V after the ultrasonic impact strengthening experiments with the 5 µm preload depth + 5 µm impact depth, 10 µm preload depth + 10 µm impact depth, 15 µm preload depth + 15 µm impact depth, respectively. It showed that the width and depth of the residual craters became larger as the preloading depth and impact depth increased. In the meantime, it was apparent that the plastic flow characteristic of Ti-6Al-4V led to the pile-up of material on both sides of the crater. After the ultrasonic impact strengthening experiments, the width and depth of the residual craters on the surface of Ti-6Al-4V were measured, and the results are shown in Fig. 20. As for the experimental parameter of 5 µm impact depth based on 5 µm preload depth (5 µm preload depth + 5 µm impact depth), the width and depth of the crater were about 200 µm and 0.92 µm, respectively. Comparing with the condition of 5 µm impact depth, the width and depth of the residual crater were improved by 38.6% and 133%, respectively. As for the experimental
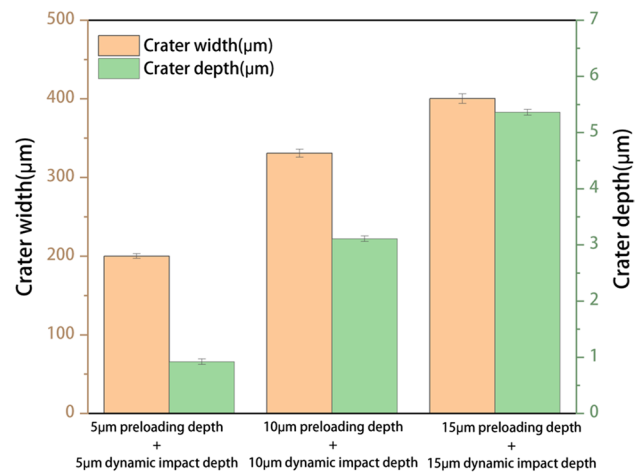

Fig. 20 Width and depth of the residual craters at different ultrasonic impact strengthening parameters

parameter of 10 µm impact depth based on 10 µm preload depth (10 µm preload depth + 10 µm impact depth), the width and depth of the crater were about 330 µm and 3.10 µm, respectively. Comparing with the condition of 10 µm impact depth, the width and depth of the residual crater were improved by 57.8% and 189%, respectively. As for the experimental parameter of 15 µm impact depth based on 15
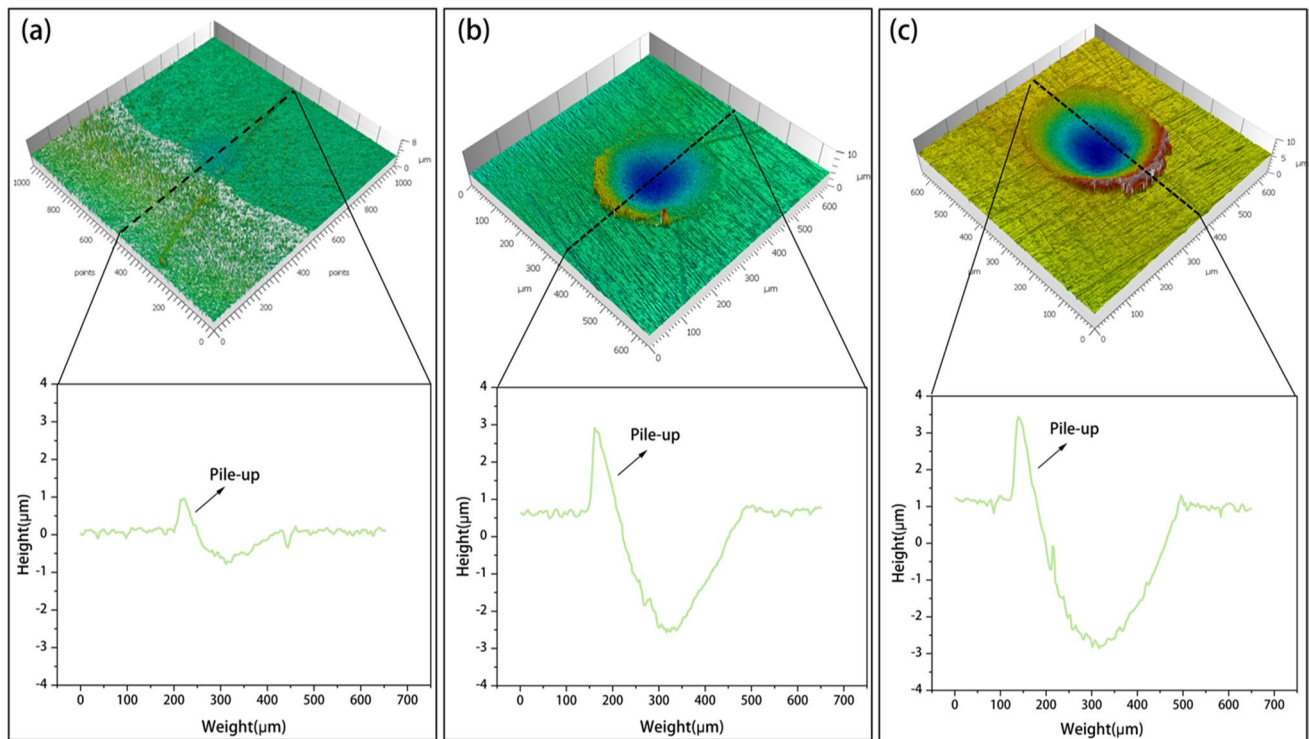

Fig. 19 Surface images and cross-sectional profiles of the craters under different ultrasonic impact strengthening parameters: **a** 5 µm preload depth + 5 µm impact depth; **b** 10 µm preload depth + 10 µm impact depth; **c** 15 µm preload depth + 15 µm impact depth

μm preload depth (15 μm preload depth + 15 μm impact depth), the width and depth of the crater were about 403 μm and 5.35 μm, respectively. Comparing with the condition of 15 μm impact depth, the width and depth of the residual crater were improved by 59.2% and 190%, respectively.

Figure 21 shows the surface morphology of the craters after the ultrasonic impact strengthening experiments with the 5 μm preload depth + 5 μm impact depth, 10 μm preload depth + 10 μm impact depth, and 15 μm preload depth + 15 μm impact depth, respectively. It found that there were two distinct regions appeared inside the craters after the ultrasonic impact strengthening experiments. Moreover, according to the different characteristic of the surface integrity, the contact area inside the crater could be divided into two regions. In Region 1, the deformation behavior of Ti-6Al-4V was defined as the undesirable plastic flow. This could induce the accumulation of misfolded of the plastic deformation layer, which leading to the poor surface integrity. In Region 2, the deformation behavior of Ti-6Al-4V was defined as the desirable plastic flow. It was observed that the surface in this region was very smooth. Furthermore, the surface integrity was significantly better than that of Region 1.

4 Conclusions

In this paper, an ultrasonic impact-strengthening test platform was developed to investigate the influence mechanisms of static loads and cyclic dynamic impact loads in the ultrasonic impact-strengthening process of Ti-6Al-4V. Based on this developed test platform, the force of ultrasonic impact strengthening were measured using a high-sensitivity force sensor with a high natural frequency. This study provide guidance and optimizing methods to the process parameters of the ultrasonic impact strengthening and the ultrasonic vibration-assisted machining. The conclusions are as follows:

1. For the ultrasonic impact strengthening experiment, the force value in the ultrasonic impact strengthening process is not only the superposition of the static load force and the impact load force, but indicating a coupling effect. The force of ultrasonic impact strengthening process increased by more than 55% compared to the sum of the static load and the maximum dynamic impact load. The degree of coupling effect becomes more obvious under the condition of the deeper press-in depth and the larger impact amplitude.
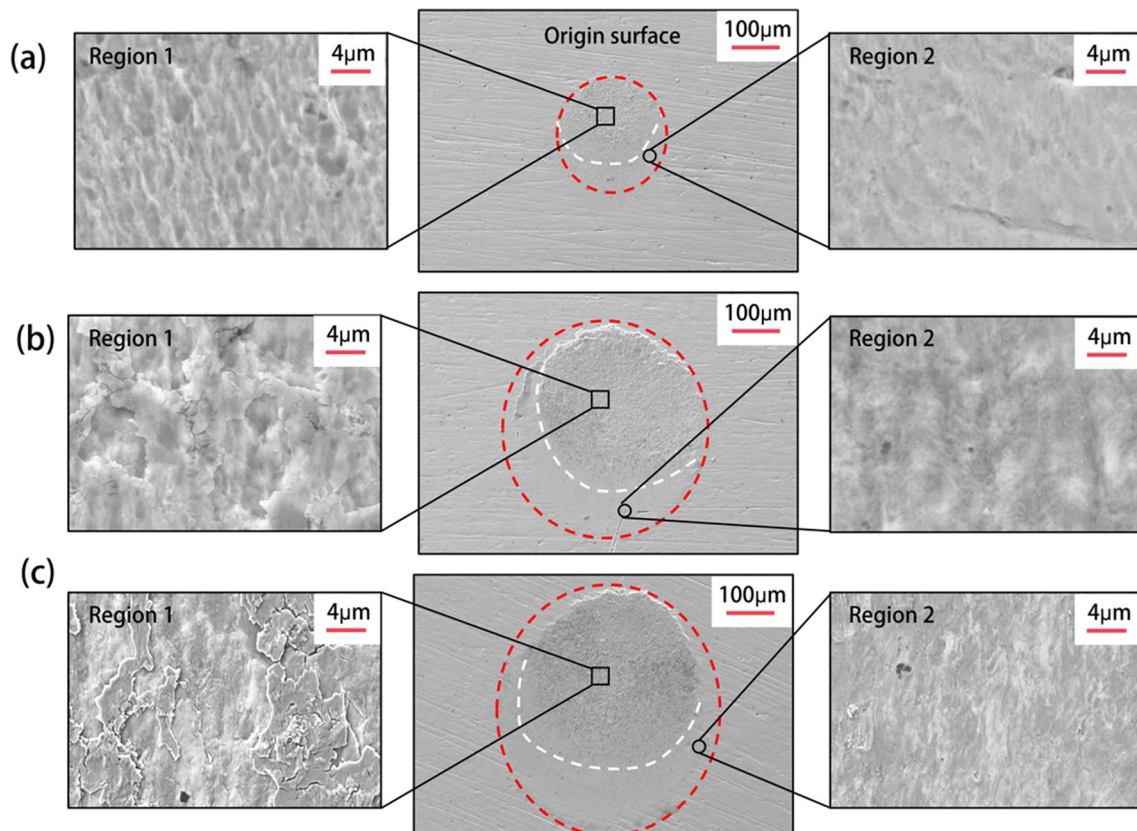

Fig. 21 Surface morphology of the craters under different ultrasonic impact strengthening parameters: **a** 5 μm preload depth + 5 μm impact depth; **b** 10 μm preload depth + 10 μm impact depth; **c** 15 μm preload depth + 15 μm impact depth

2. The dynamic impact loading induced the high velocities and accelerations. This could increase the plastic deformation strain rate of Ti-6Al-4V and lead to the material embrittlement. There is a positive correlation between the impact depth and plastic deformation strain rate of Ti-6Al-4V. During the ultrasonic impact strengthening process, the deformation strain rate of Ti-6Al-4V could reach 960 s^{-1}, 1587 s^{-1}, and 2043 s^{-1} when the cyclic impact depths of 5 µm, 10 µm, and 15 µm, respectively. The hardness of Ti-6Al-4V after the ultrasonic impact-strengthening process increased by more than 11% compared to the original hardness. It can be inferred that when the cyclic dynamic impact loading applied base on a static loading, this static preload is conducive to the energy transmission between the tool and material during the ultrasonic impact-strengthening process. It could cause a larger plastic deformation strain rate and material embrittlement effect.

3. The high temperature occurred in the contact area during the ultrasonic impact-strengthening process. Under the condition of high temperature and intense friction, the oxidation and adhesion effect of Ti-6Al-4V has emerged gradually, and this action grew more intense.

4. There were two distinct regions appeared inside the craters after the ultrasonic impact strengthening experiments. According to the different characteristic of the surface integrity, the contact area inside the crater could be divided into two regions. In one region, the deformation behavior of Ti-6Al-4V was defined as the undesirable plastic flow. This could induce the accumulation of misfolded of the plastic deformation layer, which leads to the poor surface integrity. In the other region, the deformation behavior of Ti-6Al-4V was defined as the desirable plastic flow. The surface was very smooth and the surface integrity was significantly better.

Declarations

Conflict of interest The authors declare no competing interests.

References

1. Han Q, Lei X, Yang H et al (2021) Effects of temperature and load on fretting fatigue induced geometrically necessary dislocation distribution in titanium alloy. Mater Sci Eng A 800:140308

2. Lavella M, Botto D (2018) Fretting fatigue analysis of additively manufactured blade root made of intermetallic Ti-48Al-2Cr-2Nb alloy at high temperature. Materials 11(7):1052

3. Xu Y, Cheng L, Shu C et al (2020) Foreign object damage performance and constitutive modeling of titanium alloy blade. Int J Aerosp Eng. https://doi.org/10.1155/2020/2739131

4. Zhao Q, Sun Q, Xin S et al (2022) High-strength titanium alloys for aerospace engineering applications: A review on melting-forging process. Mater Sci Eng A 143260

5. Arrazola PJ, Garay A, Iriarte LM et al (2009) Machinability of titanium alloys (Ti6Al4V and Ti555.3). J Mater Process Technol 209(5):2223–2230

6. Fouvry S, Arnaud P, Mignot A et al (2017) Contact size, frequency and cyclic normal force effects on Ti–6Al–4V fretting wear processes: an approach combining friction power and contact oxygenation. Tribol Int 113:460–473

7. Liu R, Yuan S, Lin N et al (2021) Application of ultrasonic nanocrystal surface modification (UNSM) technique for surface strengthening of titanium and titanium alloys: a mini review. J Mater Res Technol 11:351–377

8. Unal O, Varol R (2015) Surface severe plastic deformation of AISI 304 via conventional shot peening, severe shot peening and repeening. Appl Surf Sci 351:289–295

9. Statnikov ES, Korolkov OV, Vityazev VN (2006) Physics and mechanism of ultrasonic impact. Ultrasonics 44:e533–e538

10. Peyre P, Fabbro R (1995) Laser shock processing: a review of the physics and applications. Opt Quantum Electron 27:1213–1229

11. Liu YH, Zhang DY, Geng DX et al (2023) Ironing effect on surface integrity and fatigue behavior during ultrasonic peening drilling of Ti-6Al-4V. Chinese J Aeronaut. https://doi.org/10.1016/j.cja.2022.12.009

12. Yang Y, Yang M, Li C et al (2023) Machinability of ultrasonic vibration-assisted micro-grinding in biological bone using nanolubricant. Front Mech Eng 18(1):1–16

13. Jia D, Li C, Zhang Y et al (2019) Experimental evaluation of surface topographies of NMQL grinding ZrO_2 ceramics combining multiangle ultrasonic vibration. Int J Adv Manuf Technol 100:457–473

14. Gao T, Zhang X, Li C et al (2020) Surface morphology evaluation of multi-angle 2D ultrasonic vibration integrated with nanofluid minimum quantity lubrication grinding. J Manuf Process 51:44–61

15. Hudis M (1973) Study of ion-nitriding. J Appl Phys 44(4):1489–1496

16. Pham XD, Hoang AT, Nguyen DN et al (2017) Effect of factors on the hydrogen composition in the carburizing process. Int J Appl Eng Res 12(19):8238–8244

17. Zhang Q, Hu Z, Su W et al (2017) Microstructure and surface properties of 17-4PH stainless steel by ultrasonic surface rolling technology. Surf Coat Technol 321:64–73

18. Liu C, Liu D, Zhang X et al (2019) Improving fatigue performance of Ti-6Al-4V alloy via ultrasonic surface rolling process. J Mater Sci Technol 35(8):1555–1562

19. Sun Q, Yang M, Jiang Y et al (2022) Achieving excellent corrosion resistance properties of 7075 Al alloy via ultrasonic surface rolling treatment. J Alloys Compd 911:165009

20. Zheng GY, Luo X, Huang B et al (2021) Distributions of grains and precipitates in gradient lamellae Al–Zn–Mg–Cu alloy by ultrasonic surface rolling processing. Mater Sci Eng A 825:141911

21. Chen D, Hu Y, Guo L et al (2022) The modified wear resistance of uranium induced by ultrasonic surface rolling process. Wear 502:204390

22. Ma C, Suslov S, Ye C et al (2019) Improving plasticity of metallic glass by electropulsing-assisted surface severe plastic deformation. Mater Des 165:107581

23. Meng Y, Deng J, Wu J et al (2022) Improved interfacial adhesion of AlTiN coating by micro-grooves using ultrasonic surface rolling processing. J Mater Process Technol 304:117570

24. Ye H, Sun X, Liu Y et al (2019) Effect of ultrasonic surface rolling process on mechanical properties and corrosion resistance of AZ31B Mg alloy. Surf Coat Technol 372:288–298

25. Miller DA, Lagoudas DC (2001) Influence of cold work and heat treatment on the shape memory effect and plastic strain development of NiTi. Mater Sci Eng A 308(1-2):161–175

26. Zhang Y, Li C, Ji H et al (2017) Analysis of grinding mechanics and improved predictive force model based on material-removal and plastic-stacking mechanisms. Int J Mach Tools Manuf 122:81–97

27. Li C, Piao Y, Meng B et al (2022) Phase transition and plastic deformation mechanisms induced by self-rotating grinding of GaN single crystals. Int J Mach Tools Manuf 172:103827

28. Li C, Wu Y, Li X et al (2020) Deformation characteristics and surface generation modelling of crack-free grinding of GGG single crystals. J Mater Process Technol 279:116577

29. Hansen N.. Hall–Petch Relation and Boundary Strengthening. Scr Mater, 2004, 51(8): 801-806.

30. Johnson GR, Cook WH (1985) Fracture characteristics of three metals subjected to various strains, strain rates, temperatures and pressures. Eng Fract Mech 21(1):31–48

31. Hou Y, Tie Y, Li C et al (2019) Low-velocity impact behaviors of repaired CFRP laminates: Effect of impact location and external patch configurations. Compos B Eng 163:669–680

32. Zhang M, Deng J, Liu Z et al (2019) Investigation into contributions of static and dynamic loads to compressive residual stress fields caused by ultrasonic surface rolling. Int J Mech Sci 163:105144

33. Liu Y, Zhao X, Wang D (2014) Effective FE model to predict surface layer characteristics of ultrasonic surface rolling with experimental validation. Mater Sci Technol 30(6):627–636

34. Khan MK, Fitzpatrick ME, Wang QY et al (2018) Effect of ultrasonic nanocrystal surface modification on residual stress and fatigue cracking in engineering alloys. Fatigue Fract Eng Mater Struct 41(4):844–855

35. Zha X, Jiang F, Xu X (2017) Investigation of modelling and stress distribution of a coating/substrate system after an indentation test. Int J Mech Sci 134:1–14

36. Sun Z, Geng D, Zheng W et al (2023) An innovative study on high-performance milling of carbon fiber reinforced plastic by combining ultrasonic vibration assistance and optimized tool structures. J Mater Res Technol 22:2131–2146

37. Zha X, Jiang F, Xu X (2018) Investigating the high frequency fatigue failure mechanisms of mono and multilayer PVD coatings by the cyclic impact tests. Surf Coat Technol 344:689–701

38. Zha X, Chen F, Jiang F et al (2019) Correlation of the fatigue impact resistance of bilayer and nanolayered PVD coatings with their cutting performance in machining Ti6Al4V. Ceram Int 45(12):14704–14717

39. Zha X, Wang T, Chen F et al (2022) Investigation of the fatigue impact behavior and wear mechanisms of bilayer micro-structured and multilayer nano-structured coatings on cemented carbide tools in milling titanium alloy. Int J Refract Hard Met 103:105738

40. Yang X, Zhang B (2019) Material embrittlement in high strain-rate loading. Int J Extreme Manuf 1(2):022003

41. Zhang T, Jiang F, Huang H et al (2021) Towards understanding the brittle–ductile transition in the extreme manufacturing. Int J Extreme Manuf 3(2):022001

42. Ren Z, Li Z, Zhou S et al (2022) Study on surface properties of Ti-6Al-4V titanium alloy by ultrasonic rolling. Simul Model Pract Theory 121:102643

43. Guo P, Zhao Y, Zeng W et al (2013) The effect of microstructure on the mechanical properties of TC4-DT titanium alloys. Mater Sci Eng A 563:106–111

44. Sumiya H, Uesaka S, Satoh S (2000) Mechanical properties of high purity polycrystalline cBN synthesized by direct conversion sintering method. J Mater Sci 35:1181–1186

45. Wang YM, Ma E (2003) Temperature and strain rate effects on the strength and ductility of nanostructured copper. Appl Phys Lett 83(15):3165–3167

46. Ritchie RO (2011) The conflicts between strength and toughness. Nat Mater 10(11):817–822

47. Cahoon JR, Broughton WH, Kutzak AR (1971) The determination of yield strength from hardness measurements. Metall Trans 2:1979–1983